Realizing High-Efficiency Omnidirectional n-Type Si Solar Cells *via* the Hierarchical Architecture Concept with Radial Junctions

Hsin-Ping Wang,[†] Tzu-Yin Lin,[†] Chia-Wei Hsu,[‡] Meng-Lin Tsai,[†] Chih-Hsiung Huang,[†] Wan-Rou Wei,[†] Ming-Yi Huang,[§] Yi-Jiunn Chien,[§] Po-Chuan Yang,[§] Chee-Wee Liu,[†] Li-Jen Chou,[‡] and Jr-Hau He[†,*]

[†]Institute of Photonics and Optoelectronics & Department of Electrical Engineering, National Taiwan University, Taipei 10617, Taiwan, [‡]Department of Materials Science and Engineering, National Tsing Hua University, Hsinchu 30013, Taiwan, and [§]Advanced Technology Department, AU Optronic Corporation, Taichung 40763, Taiwan

ABSTRACT Hierarchical structures combining micropyramids and nanowires with appropriate control of surface carrier recombination represent a class of architectures for radial p-n junction solar cells that synergizes the advantageous features including excellent broad-band, omnidirectional light-harvesting and efficient separation/collection of photoexcited carriers. The heterojunction solar cells fabricated with hierarchical structures exhibit the efficiency of 15.14% using cost-effective as-cut Czochralski n-type Si substrates, which is the highest reported efficiency among all n-type Si nanostructured solar cells. We also demonstrate the omnidirectional solar cell that exhibits the daily generated power enhancement of 44.2% by using hierarchical structures, as compared to conventional micropyramid control cells. The concurrent improvement in optical and electrical properties for realizing high-efficiency omnidirectional solar cells using as-cut Czochralski n-type Si substrates demonstrated here makes a hierarchical architecture concept promising for large-area and cost-effective mass production.

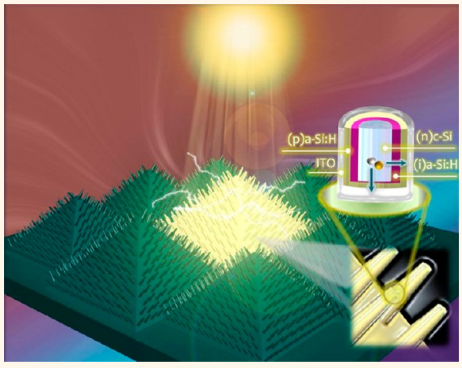

KEYWORDS: photon management · high-efficiency · hierarchical architecture · radial junctions · omnidirectional · Si heterojunction (SHJ) solar cells · chemical polishing etching

Photon management for smart control of light by employing nanostructures has attracted considerable attention for boosting the efficiency of optoelectronic devices including photodetectors,[1,2] light-emitting diodes,[3] and solar cells.[4−7] It has been reported that by controlling light at the nanometer scale using nanostructures, coupled with emerging materials fabrication approaches, theoretically allows the development of solar cells with efficiencies in the 50−70% range, breaking the Shockley−Queisser limit.[7] It is because nanostructures are expected to have a great potential in improving both optical and electrical characteristics of cells. First, with the deliberate geometry design (including diameter,[8] length,[9] surface profile,[10] and interface roughness control),[11] the nanostructures can significantly suppress the reflectance and efficiently enhance the light propagation length of guided mode couplings in wide ranges of wavelengths. Second, from the electrical viewpoint, provided by radial p-n junction design of high-aspect-ratio nanostructures, photoexcited carriers are collected along the radial direction while photons are absorbed along the nanowires (NWs), providing a carrier collection path separated from the photon absorption thickness. Thus, photoexcited carriers can efficiently diffuse over a short distance to the junction and can be extracted with minimal recombination.[6,12,13]

Despite the above-mentioned potential advantages inspired by the radial p-n junction structure, most studies in nanostructured solar cells show device performance degradation in spite of strong optical enhancement. To exploit these advantages in practice, there are still key design challenges yet to be addressed and aspects to be considered. In particular, although photoexcited carriers can rapidly transport

* Address correspondence to jhhe@cc.ee.ntu.edu.tw.

Received for review August 1, 2013 and accepted September 18, 2013.

Published online September 18, 2013
10.1021/nn404015y

© 2013 American Chemical Society

to the junction interface, these carriers are easily trapped by high-density surface defects (caused by the ultrahigh surface area as prolonging the length of NWs) before being collected by the external circuit. High recombination velocity caused by high-density surface defects would sacrifice electrical advantages of radial junction architecture and thus lead to the performance deterioration including low open-circuit voltages (V_{oc}), short-circuit current (J_{sc}), and fill factor (FF).[14−18] Accordingly, a concurrent improvement in electrical and optical characteristics of the radial junction architecture is the most important issue for putting high-efficiency nanostructured solar cells into practice.

In the past decade, n-type Si solar cells have drawn intensive interest.[19] A world-record high efficiency of 24.7% utilizing Panasonic's heterojunction with intrinsic thin-layer (as known as HIT) technology among all kinds of Si-based solar cells of practical size (100 cm^2 and above) has been achieved with a 98 μm thick Czochralski (Cz) n-type monocrystalline Si cell in February of 2013.[20] Although currently p-type Si is the most common photovoltaic (PV) material (for example, 84% of PV module production in 2011), several fundamental advantages warrant n-type Si solar cells having large potential to surpass p-type Si solar cells in terms of efficiency and cost effectiveness: (i) suitable band structure for high-efficiency n-type Si heterojunction (SHJ) solar cells;[21] (ii) high minority carrier lifetimes up to the millisecond range, which is important for photoexcited carrier collection;[22] (iii) no light-induced degradation caused by boron−oxygen pair;[23] (iv) high impurity tolerance, allowing the use of cost-effective Cz wafers.[24] While the scientists around the world are starting to pay more attention to nanostructured solar cells using n-type Si, the PV characteristics of n-type Si nanostructured solar cells obtained have been worse than expected. Representative progresses on n-type Si nanostructured solar cells are summarized in Table S1 in Supporting Information.

It is known that the angle of incidence (AOI) of the sun changes during a day and sunlight reaching the earth is a mixture of direct and scattered (diffuse) radiation after passing through the atmosphere. Moreover, on cloudy days, the light consists principally of diffuse radiation (over 90%). For a polished Si surface, nearly 40% of light is reflected when averaged over all AOIs and the solar spectrum (400−1100 nm).[25] For most conventional cells with micropyramid (MP) structures, the reflectance is strongly angular-dependent due to the pyramid architecture resulting in insufficient light trapping. Typically, to surpass the directional dependence of PV performance, expensive sun-tracking systems continuously changing direction during the day to optimally collect sunlight are used for solar cell panels. One should note that most sun-tracking systems utilize direct radiation only; that is, these tracking systems work well on bright clear days but poorly on hazy days. Furthermore, additional expensive tracking systems are not suitable for cost-effective Si-based solar cells. To reduce the number of these "wasted photons" caused by the effect of AOIs, it is critical to develop omnidirectional solar cells. With better omnidirectional light-harvesting ability, more daily generation power is expected. To date, most studies in photon management using nanostructures only reported omnidirectional optical effects, and few studies readily realized omnidirectional light-harvesting solar cells.[8,11]

In this study, the photon management using the hierarchical structures combining MPs and NWs shows excellent light-harvesting characteristics; the hierarchical structures with only 1.16 μm length NWs can suppress the total reflection to 2.96% with wavelengths of 300−1100 nm, even superior to the surfaces purely consisting of long NWs with up to 40 μm in length.[9] A key optical benefit of the hierarchical architecture design stems from the multiple scattering effect of MPs and the gradient refractive index effect of NWs, allowing more photons to enter the entire devices. We have chosen SHJ solar cells using as-cut Cz n-type substrates with hydrogenated amorphous Si (a-Si:H) layers to demonstrate the hierarchical architecture concept with radial junctions. Applying the chemical polishing etching (CPE) treatment to the hierarchical structures leads to atomically smooth and contamination-free surface, avoiding the nonconformal a-Si:H and metal deposition and the excessive carrier trapping centers caused by a high density of surface defects and metal contamination as in the high-aspect-ratio nanostructures. These concurrent improvements in optical and electrical design of hierarchical structures reflect their success in the practical SHJ cells, which achieve J_{sc} of 36.58 mA/cm^2, V_{oc} of 595.65 mV, FF of 69.5%, and thus efficiency of 15.14%. Excitingly, excellent omnidirectional PV characteristics are also achieved with the hierarchical structures. The specular reflectance is less than 0.23% for all the wavelengths at the AOI up to 70°, which directly leads to excellent omnidirectional PV characteristics of SHJ cells with hierarchical structures; that is, the daily power density enhancement (44.2%) is 2 times higher than the power density enhancement at normal AOI (21.8%), as compared to conventional MP control cells. The realization of high-efficiency omnidirectional solar cells using as-cut Cz n-type substrates demonstrated here makes hierarchical concepts attractive for large-area and cost-effective production.

RESULTS AND DISCUSSION

Figure 1a−c shows the schematic and the scanning electron microscopy (SEM) images (recorded at the tilted angle of 45°), indicating the morphology evolutions in the etching process for the formation of

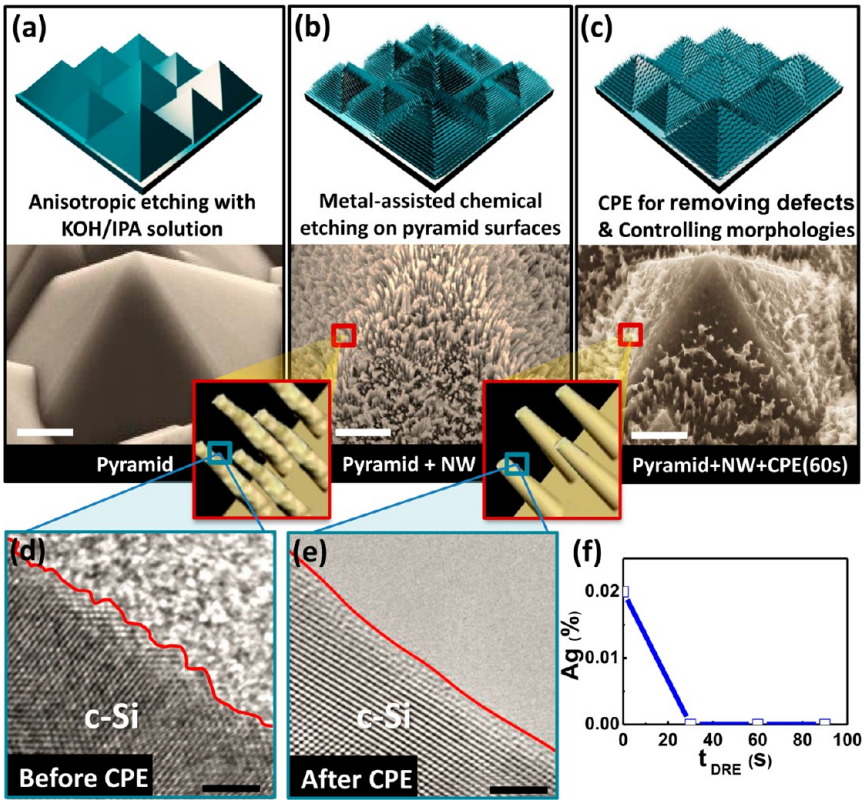

Figure 1. (a–c) Schematics of the corresponding experimental procedures and corresponding SEM images. The scale bars in (a–c) represent 3 μm. HRTEM images taken near the edge of the individual NW on hierarchical structures (d) before and (e) after the CPE treatment. The scale bars in (d,e) represent 3 nm. (f) Ag concentration as a function of time for CPE treatment with the hierarchical structure surfaces obtained from Ag 3d XPS spectra from Figure S2.

hierarchical Si surfaces composed of microscale and nanoscale structures. First, the Si MPs were fabricated on as-cut monocrystalline n-type Cz Si (001) wafers *via* an anisotropic etching process with a solution of potassium hydroxide (KOH) and isopropyl alcohol (IPA). Note that for large-scale solar cell production, the Cz wafer is preferred because of its cost effectiveness, although float-zoning Si exhibits higher carrier lifetimes and thus higher expected efficiency in most of cases.[26] Moreover, in the PV industry, as-cut wafers without chemical mechanical polishing are usually directly used for excluding the polishing cost in the commercial cell fabrication. Therefore, as-cut n-type Cz wafers were utilized thoroughly to fabricate SHJ solar cells in this study to confirm that the concept demonstrated here can be practically turned into industry production. This is also the reason that the high-cost, low-efficiency cells with polished Si are not presented here. After 20 min anisotropic etching, MPs ranging from 7 to 12 μm in width were formed. Subsequently, the large-area uniform hierarchical structures combining MPs and NWs were obtained by metal-assisted chemical etching on micropyramidal surfaces for 30 s, as shown in Figure 1b. Finally, the CPE was carried out to reduce the surface defects and control the final morphologies. The CPE solution is the mixture of nitric acid (HNO_3) and hydrofluoric acid (HF). The SEM images of hierarchical structures with different durations of CPE including 0, 30, 60, and 90 s are shown in Figure S1a–d in Supporting Information, respectively. One can see that after CPE treatment, the density and the length of NWs are reduced. The density of the Si NWs on MPs is about 100.0 μm^{-2} for as-fabricated hierarchical structures and reduces to ~2.1 μm^{-2} after the CPE treatment for 60 s.

Black Si made by metal-assisted chemical etching has become popular for solar cells because of its high uniformity and easy fabrication, but it also causes additional defects in two ways, significantly degrading the cell performance. First, during the etching process, the randomness of lateral oxidation and dissolution/redeposition of Ag nanoparticles on the micropyramidal surfaces due to the redox of Ag could contribute to the atomic surface roughness, which has been characterized by transmission electron microscopy (TEM), as shown in Figure 1d.[27,28] The atomically rough surfaces causing additional surface defects are useless for light harvesting but act as the nucleation sites for epitaxial Si (epi-Si) growth during a-Si:H film growth using plasma-enhanced chemical vapor deposition (PECVD).[29] The formation of epi-Si in a-Si:H layers results in poor surface/field-effect passivation, leading to high carrier recombination rate and then severe deterioration of the V_{oc} and FF.[30,31] Second, the surface

may be contaminated by Ag^+ ions or Ag nanoparticles. The catalyst metal might diffuse into Si surfaces during the formation of NWs *via* a metal-assisted etching process. Previously, HNO_3 solution has been used to clean the residual Ag after NW formation.[8] However, Ag nanoparticles may not be completely removed by HNO_3 cleaning due to the hydrophobicity of etched Si surfaces and thus remain in the bottom of NWs.[32,33] The residual Ag contamination creates carrier trapping centers and reduces minority carrier lifetimes, inevitably detrimental to the Si NW devices.[34,35]

Applying the CPE (HNO_3/HF) treatment to as-fabricated hierarchical structures can concurrently relieve these two disadvantages. One of the striking features of the HNO_3/HF isotropic etching is creating the atomically smooth surface of NWs. Compared with as-fabricated hierarchical structures (Figure 1d), the significant reduction in roughness of NW surfaces by the CPE treatment is observed by TEM characterization, as shown in Figure 1e. The oxidation of Si by HNO_3 forms atomically smooth SiO_2/Si interfaces due to the volume expansion during the oxidation. Consequently, the atomically smooth Si surfaces are exposed after etching off SiO_2 layers with HF and thus expected to avoid the epi-Si growth during a-Si:H layer deposition by PECVD for fabricating SHJ cells (which will be demonstrated and discussed later).[36,37] Furthermore, one can see that after CPE, density and length of NWs are reduced, which benefits conformal deposition of the following a-Si:H and metal contact layers for fabricating SHJ cells. Moreover, with a decrease in density and length of NWs, the HNO_3 solution would easily penetrate into the bottom of NWs to completely remove the remaining Ag between NWs. Accordingly, the contaminated surface by Ag^+ or Ag nanoparticles can be moved away by the CPE treatment for hierarchical structures, confirmed by XPS analysis shown in Figure S2 in Supporting Information. From Figure 1f, the Ag content decreases from 0.02% (CPE time = 0 s) to 0% (undetectable level by XPS) (CPE time = 30 s), indicating that the Ag contamination is completely removed after 30 s CPE treatment. Briefly speaking, the atomically smooth and contamination-free NW surface can be achieved by employing the CPE treatment.

In order to evaluate the light-harvesting characteristics of hierarchical structures, the total reflectance (R_{total}) in the wavelength range of 300−1100 nm was measured, as shown in Figure 2a. In contrast to the MP structures, the as-fabricated hierarchical structures effectively reduce the reflectance over the broad-band regions and exhibit reduced average R_{total} from 19.17 to 2.96%. The superior light-harvesting property of the hierarchical structures can be attributed to two effects: the scattering effect of MPs and the gradient refractive index effect of NWs. The microscale structures cause effective multiple scattering; as incident light reaches the Si micropyramidal surfaces, it diffracts to several beams and partly rebounces between the MPs, preventing light from escaping back to air and thus increasing the probability of photons being absorbed.[38] As for the hierarchical surfaces, the subwavelength features of the NWs on the microscale pyramidal surfaces behave like an effective medium with the effective refractive index (n_{eff}) gradually decreasing toward air, further increasing the amount of photons entering the structures.[11] Due to the gradient refractive index effect combined with the scattering effect, the hierarchical structures exhibit superior light-harvesting ability.[39]

It is worth noting that the hierarchical structure combination of MPs and NWs with ~1.16 μm length shows lower reflectance than the structured surfaces purely consisting of NWs with up to 40 μm in length made by metal-assisted chemical etching.[9,40] This is an important advantage of hierarchical structures for nanostructured solar cells, which is very sensitive to the surface quality. Simply prolonging the length of NWs for increasing light-harvesting ability would simultaneously result in high surface recombination loss due to the increased surfaces, leading to unsatisfactory V_{oc} and FF.[41] Therefore, the hierarchical structure is expected to be a potential candidate exhibiting excellent photon management ability and simultaneously avoiding the severe surface recombination loss. After the formation of more polished surfaces by CPE treatments for 90 s, the average R_{total} of hierarchical structures increases from 2.96 to 13.95% but is still lower than that of micropyramidal surfaces (average R_{total} = 19.17%), as shown in Figure 2a. The light-harvesting ability can also be illustrated by the change in the sample's appearance, as shown in the photographic images (Figure 2b). Uniform color distribution suggests that the MPs or the hierarchical structures uniformly distributed on the entire 16 cm^2 samples.

In addition to the R_{total} measurement, AOI-dependent specular reflectance (R_{spec}) was measured to investigate omnidirectional light-harvesting ability of hierarchical structures, as shown in Figure 2c−g. For the micropyramidal surface, the reflectance cannot be effectively suppressed for the wavelengths lower than 500 nm at all of AOIs due to high refractive index of Si at short wavelength regions. Moreover, the reflectance is strongly angular-dependent, which is attributed to the MPs with facets at 54.7° relative to the wafer surface. As shown in Figure 2d, the R_{spec} is effectively suppressed by the hierarchical surfaces at all AOIs and incident wavelengths; the AOI limit is further pushed to 70°, below which the reflectance is less than 0.23% for all the wavelengths. Due to the formation of more polished surfaces *via* CPE treatment, the R_{spec} of hierarchical structures is increased with CPE time at all of AOIs and wavelengths. Briefly, Figure 2d−g clearly shows that the hierarchical surfaces can broad-bandly and omnidirectionally suppress the undesired Fresnel reflection.

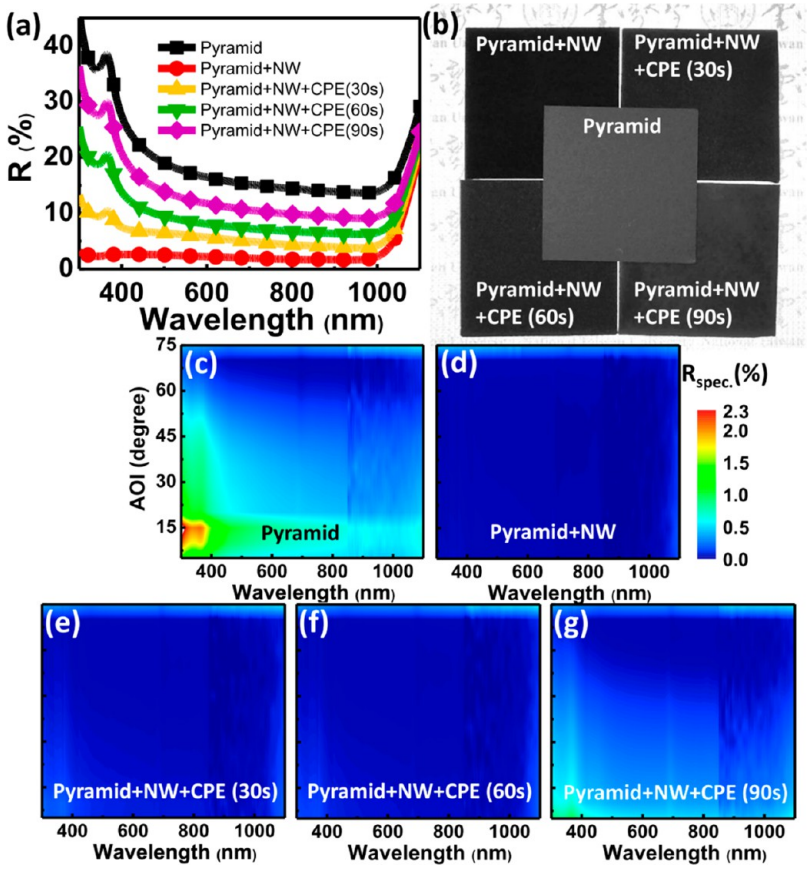

Figure 2. (a) Total reflectance spectra of MP and hierarchical structures with different CPE durations over the wavelength regions of 300−1100 nm. (b) Photographic image of five kinds of structures on 4 × 4 cm^2 wafers. Specular reflectance spectra of (c) micropyramidal surfaces and (d−g) hierarchical surfaces with different CPE durations.

The beneficial effect of the omnidirectionality characteristics of hierarchical structures on the practical solar cell performance under a variety of AOIs will be addressed later.

To gain insight into the light-harvesting ability, we simulated the light propagating across micropyramidal and hierarchical surfaces using FDTD analysis. The grid sizes are $\Delta x \times \Delta y = 0.01 \times 0.01\ \mu m^2$ in space domain, and the time step for every calculation is 0.012 fs. In the figures, the distribution of time-averaged electric field ($|E|$) in Si micropyramidal (Figure 3a) and hierarchical structures (Figure 3b) is calculated using $\lambda = 550$ nm. More details about simulated structures and optical parameters are described in Figure S3 in Supporting Information. The insets of Figure 3a,b show the high-magnification images at the interface region of air and a-Si:H/c-Si to highlight the light-harvesting effect. As compared with the MP structure, the hierarchical structure shows strong and uniform field intensities within the NWs and the MPs, demonstrating a great absorption enhancement. The NWs on the MPs guide more light propagating across the interfaces between air and MPs. Figure 3c shows the steady-state optical power detected at the a-Si:H/c-Si interface (p-n junction), integrating the power flux in the a-Si:H/c-Si interface regions, as a function of time for the two kinds of structures. The steady-state power values for two structures are 0.38 (MP) and 0.47 (hierarchical structure), which is a dramatic increase of 23.7% by introducing the hierarchical structure. The simulation findings agree with the experimental reflection results, confirming the excellent photon management characteristics of hierarchical structures.

In addition to the reflectance measurement, the effective minority carrier lifetime measurement using the quasi-steady-state photoconductance (QSSPC) technique is employed to evaluate the surface/interface defects, which greatly influence PV characteristics. The QSSPC technique is described in Supporting Information. The measured minority carrier lifetime (τ_{meas}) of whole recombination[42] can be expressed as

$$\frac{1}{\tau_{meas}} = \frac{1}{\tau_{bulk}} + \frac{1}{\tau_{diff} + \tau_{surf}} \quad (1)$$

$$\tau_{diff} = \frac{W^2}{\pi^2 D_{n,p}} \quad (2)$$

$$\tau_{surf} = \frac{W}{2S} \quad (3)$$

where τ_{bulk} is the bulk recombination lifetime, τ_{diff} is the characteristic time necessary for the carrier diffusion

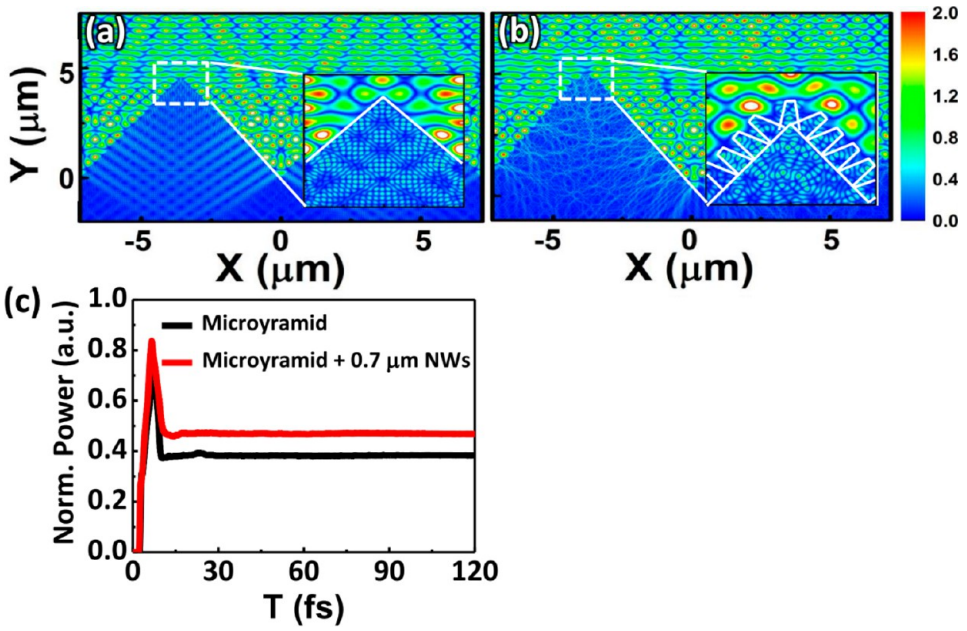

Figure 3. Time-averaged, normalized $|E|$ electric field distribution of SHJ cells with (a) MPs and (b) hierarchical structures at λ = 550 nm. (c) Simulated optical power detected at the interface between a-Si:H/c-Si.

from the middle of the wafer to the surface, τ_{surf} is the surface recombination lifetime, W is the wafer thickness, $D_{n,p}$ is the diffusion constants of minority carriers, and S is the surface recombination rate. Values of τ_{bulk} and τ_{diff} are identical for different structures as all structures are fabricated with the same wafers. Therefore, τ_{meas} changes with τ_{surf}, which is related to the surface carrier recombination. The effective minority carrier lifetime of all structures after intrinsic a-Si:H layer deposition by PECVD for passivation is shown in Figure 4a and summarized in Figure 4b at the minority carrier density of 10^{15} cm^{-3}, which is similar to the value under 1 sun illumination. One can see that the τ_{meas} greatly drops after using metal-assisted chemical etching to fabricate the hierarchical surfaces, indicating high-density surface defects and carrier trapping centers created on as-fabricated hierarchical structures' surfaces. The τ_{meas} significantly increases after applying the CPE treatment for 30 s to hierarchical structures and further increases with the duration of CPE treatment. The τ_{meas} is increased to 315.97 μs after applying CPE for 90 s at the minority carrier density of 10^{15} cm^{-3}. The increase in τ_{meas} can be attributed to the effective reduction of the surface defect and contamination and the creation of atomically smooth Si surfaces, which is also supported by TEM observation and XPS analysis (Figure 1e,f).

As shown in Figure 4c,d, the a-Si:H/c-Si interface was analyzed by TEM characterizations, indicating the NW surfaces of the hierarchical structures without and with CPE treatments after depositing a 5 nm thick intrinsic a-Si:H layer. It is noticeable that a much thinner a-Si:H layer (~3.16 nm) was observed on rough surfaces of as-fabricated hierarchical Si (Figure 4c), as compared

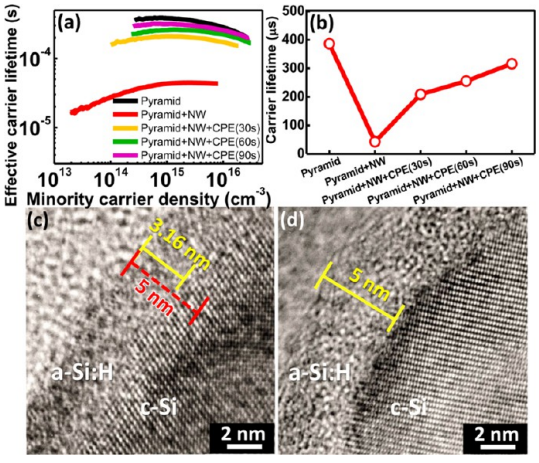

Figure 4. (a) Effective carrier lifetime as a function of minority carrier density for the MP and hierarchical structures with different CPE durations. (b) Lifetimes at carrier density of 10^{15} cm^{-3} for all structures obtained from (a). HRTEM images after a-Si:H deposition taken near the edge of the individual NW on hierarchical structures (c) without and (d) with the CPE treatment.

to ~5 nm thick a-Si:H layers obtained on the defect-removed surface of hierarchical Si after CPE treatments (Figure 4d). The difference in thickness of a-Si:H layers is attributed to the growth of epi-Si observed on rough surfaces without CPE treatments. The epi-Si is defective and comes with rough interfaces, increasing the density of other defects including dangling bonds.[31,43] Therefore, any growth of epi-Si in a-Si:H layers dramatically reduces the a-Si:H surface/field passivation ability and results in significant decrease of effective carrier lifetime.[30,31,43] As shown in Figure 4d, the CPE treatment reduces the atomic roughness and then suppresses the

epi-Si growth, obtaining the high interface passivation quality due to the formation of the defect-free abrupt a-Si:H/c-Si interface. The superior passivation quality is reflected in the increase in τ_{meas}. Briefly speaking, based on TEM observation, XPS analysis, and minority carrier lifetime measurements (Figure 4 and Figure S2 in Supporting Information), the quality of a-Si:H/c-Si interfaces can be greatly improved by applying proper CPE treatments prior to the a-Si:H passivation, which is practically beneficial to the PV performance (which will be shown later).

To evaluate the feasibility of photon management using light-harvesting hierarchical structures for converting trapped photons into electrons, all structures were fabricated to a core/shell NW solar device by PECVD processes. There are many methods to fabricate core/shell NWs. Thermal diffusion and vapor–liquid–solid growth methods are common methods for the synthesis of Si core/shell NWs. However, several challenges for practical applications using these growth methods remain. For example, when the thermal diffusion method is used to fabricate the core/shell NWs, the dopants easily diffuse into the whole NWs, avoiding the radial junction formation, losing the advantages of NW architectures (such as increased p-n junction area and effective photocarrier collection efficiency). On the other hand, when the vapor–liquid–solid growth is used to form the NWs, severe diffusion of catalyzed metal, typically Au, into Si during the NW growth is inevitable and detrimental to the realization of Si NW devices due to Au contamination in Si, creating carrier traps and reducing minority carrier lifetimes.[44] Moreover, the concentration profile of dopants is difficult to be precisely controlled at the nanoscale particularly using the high-temperature processes, such as thermal diffusion and vapor–liquid–solid growth methods. Therefore, using the PECVD method to grow the shell of NWs is a great candidate to obtain the precisely controlled and contamination-free core/shell NWs. The thickness and the dopant concentration of emitter layers can be precisely controlled by different deposition precursor, time, temperature, pressure, flow rate of gas, and power of PECVD.

All structures were fabricated with sequential SHJ solar device fabrication processes and measured under air mass 1.5 global (AM 1.5G) illumination, as shown in the current density–voltage (J–V) characterizations in Figure 5a. PV characteristics are summarized in Table 1. One can see that, although the as-fabricated hierarchical structure shows the lowest reflectance, its J_{sc} and efficiency are unsatisfactory. The poor photocarrier collection efficiency is attributed to high-density carrier trapping centers (*i.e.*, high-density surface defects, Ag contamination, and epi-Si formation during a-Si:H growth using PECVD). Moreover, the high density of defects causes many parallel paths across each layer, resulting in low shunt resistance of the solar cells.

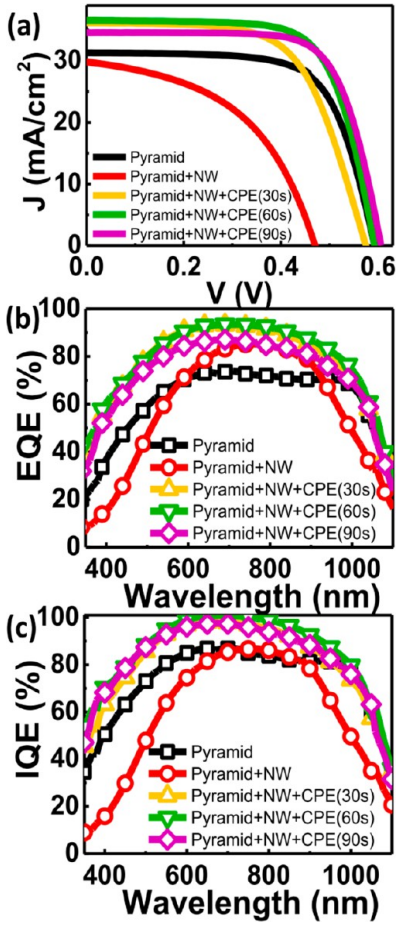

Figure 5. (a) J–V characteristics, (b) EQE spectra, and (c) IQE spectra of SHJ solar cells with different structures under AM 1.5G illumination.

TABLE 1. Characteristics of SHJ Solar Cells with Different Structures

	J_{sc} (mA/cm^2)	V_{oc} (mV)	FF (%)	eff (%)
pyramid	31.29	593.43	67.02	12.43
pyramid + NW	29.83	469.54	47.68	6.68
pyramid + NW + CPE (30 s)	36.16	574.56	62.62	13.01
pyramid + NW + CPE (60 s)	36.58	595.65	69.50	15.14
pyramid + NW + CPE (90 s)	34.57	605.97	71.27	14.93

The detrimentally low shunt resistance decreases the FF and the efficiency of a solar cell, accordingly. J_{sc}, V_{oc}, and FF show pronounced improvements after the appropriate CPE treatment. The J_{sc} of the solar cell with hierarchical structures is increased from 31.29 (MPs) to 36.58 mA/cm^2 using the CPE treatment for 60 s and slightly decreased after CPE treatment for 90 s due to the formation of relatively polished surfaces and the decrease in junction area. The continuous increase in V_{oc} and FF can be explained by (i) the removal of surface defects/contamination and the suppression of epi-Si growth after CPE treatment and (ii) the improved a-Si:H and metal film coverage on hierarchical structures due to atomically smooth surfaces and decreased

density and length of NWs *via* CPE treatments. Therefore, the compromise among light harvesting, junction area, and carrier lifetime leads to the highest conversion efficiency of 15.14% with 21.8% enhancement for hierarchical structured SHJ cells with appropriate CPE treatments, as compared to the MP cells. This also leads us to conclude that only when the carrier trapping centers are eliminated by CPE treatments can the hierarchical structures practically enjoy the advantage of excellent light-harvesting characteristics, giving rise to the significant efficiency improvement.

To gain insight into the correlation between J_{sc} enhancement and optical harvesting/carrier collection enhancement with hierarchical structures, external quantum efficiency (EQE) and internal quantum efficiency (IQE) spectra are further analyzed (Figure 5b,c). The EQE measurement indicates that, as compared to the MP device, the device with as-fabricated hierarchical structures shows pronounced EQE enhancement in the spectral region of 590 to 920 nm but efficiency degradation in short (from 300 to 590 nm) and long (from 920 to 1100 nm) wavelength regions in spite of the excellent photon management ability demonstrated in reflection measurements (Figure 2). The results prove that the main problem of unsatisfied J_{sc} and efficiency in nanostructured solar cells is from their electrical properties (*i.e.*, poor photoexcited carrier collection efficiency). After the CPE treatment is employed, EQE is increased in a wide wavelength range. Considering the fraction of the actually absorbed photons by the active layers, the EQE can be converted into the IQE, which is the ratio between the measured J_{sc} and the number of absorbed AM 1.5G photons per unit area and time. The IQE measurement is useful to exclude the optical effect for investigating the carrier collection efficiency. The surface recombination effect strongly affects the IQE at short wavelength regions since high-energy photons are absorbed near the surface.[45] Usually, nanostructured solar cells show a high surface recombination rate due to the defective surfaces and the ultrahigh surface-to-volume ratio of nanostructures, leading to poor blue spectral response.[16] Moreover, a considerable loss of long-wavelength photoexcited carriers has been observed due to the back surface recombination.[45,46] During the metal-assisted chemical etching processes, some Ag particles (Ag^+/Ag, redox potential of 0.80 V *vs* normal hydrogen electrode (NHE)) might be oxidized and dissolved into the solution due to low redox potential compared with H_2O_2 (redox potential of 1.72 V *vs* NHE in a solution at pH = 0.3), and then the Ag^+ redeposits on the Si surface not only on the top side but also on the back side.[8] The dissolution and the redeposition of Ag nanoparticles on the structures contribute to the atomic surface roughness, easily inducing epi-Si growth between a-Si:H and c-Si interface during the a-Si:H deposition process. Therefore, the IQE drops greatly at long-wavelength ranges after the metal-assisted chemical etching process. The IQE drop limits J_{sc} and overall efficiency. In this study, the CPE treatment of the hierarchical structures greatly improves the conversion efficiency of SHJ cells at short and long wavelength regions by improving nanostructured interfaces and back surface conditions of Si. The change of IQE with CPE time indicates that the surface defects can be effectively reduced even for a short period of CPE treatment time, echoing the results of the effective lifetime measurements (Figure 4). After carefully removing the surface defects, the radial junction design would be able to effectively work for the carrier collection.

To envision concurrent enhancement in V_{oc} and J_{sc} of SHJ solar cells with photon management employing hierarchical light-harvesting structures, we gain insight into implied V_{oc}, which can be used to identify the ideal device performance (assuming no electrical losses in subsequent semiconductor and metal layers (n-type and p-type a-Si:H and ITO) and contacts between these layers) for process monitoring. The minority carrier lifetime measurements allow the extraction of the implied V_{oc}. The implied V_{oc} is estimated from the equation[47]

$$j_{ph} = \frac{q\Delta n_{av} W}{\tau_{eff}} \tag{4}$$

$$\text{implied } V_{oc} = \frac{kT}{q} \ln\left(\frac{\Delta n(N_{D,A} + \Delta n)}{n_i^2}\right) \tag{5}$$

where j_{ph} is the photoexcited current, q is the charge of the electron, Δn_{av} is the average density of minority charge carriers, W is the wafer thickness, τ_{eff} is the effective carrier lifetime, k is the Boltzmann constant, T is the temperature, $N_{D,A}$ is the donor or acceptor concentration of the wafer, Δn is the excess carrier concentration, and n_i is the intrinsic carrier concentration. Under open-circuit conditions, the recombination current has to balance the photoexcited current ($j_{rec} = j_{ph}$); Δn_{av} would be similar to the value of Δn when the wafer surface is well-passivated and the wafer thickness is smaller than carrier diffusion length. Then, with a given j_{ph}, implied V_{oc} can be calculated by replacing Δn_{av} with Δn. As indicated in Figure S4 in Supporting Information, the implied V_{oc} shows the same tendency with τ_{meas}, and the implied V_{oc} of hierarchical structures with 90 s CPE treatment is almost the same as that of MPs, making the high-efficiency nanostructured SHJ solar cells possible to achieve. As compared to V_{oc} obtained from $J-V$ curves under AM 1.5G illumination, the implied V_{oc} is as high as 660 mV, indicating that V_{oc} can be improved further by optimizing the cell fabrication process for boosting the efficiency of hierarchical structured cells, which is currently under investigation.

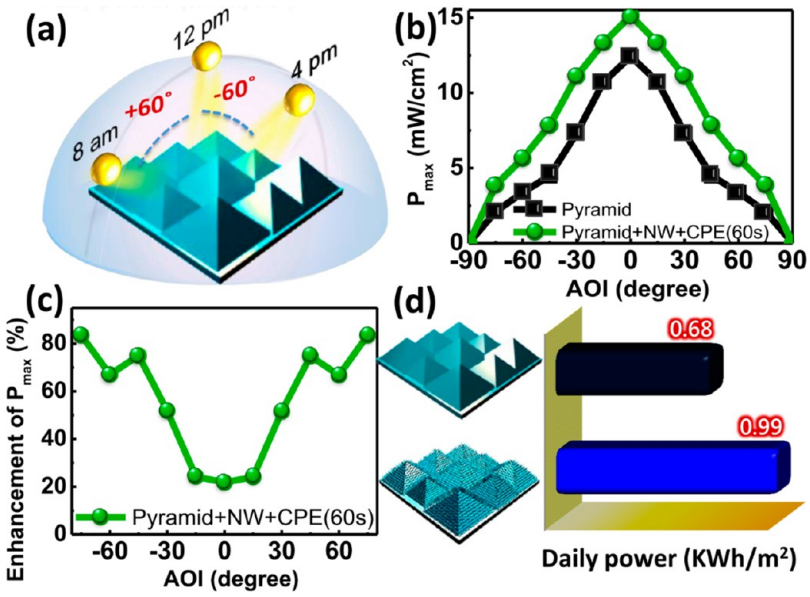

Figure 6. (a) Schematic of incident angle-dependent power generation over a day. (b) Incident angle dependence of generated maximum power. (c) Enhancement of generated maximum power. (d) Estimated average daily power density generated from the devices.

The above-discussed PV characterizations were all performed with normal incident light. However, light absorption from a variety of AOIs has to be considered for practical PV applications. We measured AOI-dependent maximum power density ($P_{max} = J_{sc} \times V_{oc} \times FF$) from −90 to 90° under AM 1.5G illumination to emphasize excellent omnidirectional PV characteristics of hierarchical structures (Figure 6a,b). To assess the omnidirectional light-harvesting enhancement, we define the P_{max} enhancement as $(P_{max,hierarchical} - P_{max,pyramid})/P_{max,pyramid}$, where $P_{max,pyramid}$ and $P_{max,hierarchical}$ are P_{max} of SHJ solar cells with MPs and hierarchical structures, respectively. As shown in Figure 6c, for SHJ cells with hierarchical surfaces, the P_{max} enhancement is 21.8% at normal incidence while increasing to 83.5% at the AOI = 75°, implying that the hierarchical structured solar cell exhibits much better light-harvesting capability at high AOI values than the MP solar cells, echoing the experimental omnidirectional reflection results (Figure 2c−g). We note that the solar spectrum changes with time of day, season, altitude, and location. Here, we performed day-integrated solar energy generation analysis (Figure 6d), in which we assume that (i) the device and the sun are confined within the equatorial plane, (ii) the *x*-axes of Figure 6b,c are both positive and negative angular ranges of the sun's movement, and (iii) the integrated P_{max} at the AOI from −90 to 90° represents the average daily power density generated from the solar cells. MP and hierarchical structured SHJ devices exhibit an integrated daily power density of 0.68 and 0.99 KWh/m^2, indicating the 44.2% enhancement after employing the hierarchical structures. Moreover, the daily power density enhancement (44.2%) is 2 times higher than the power density enhancement at normal AOI (21.8%), demonstrating the omnidirectional solar cells achieved by photon management employing hierarchical structures.

CONCLUSIONS

We demonstrated omnidirectional SHJ solar cells with n-type Si exhibiting the efficiency up to 15.14% using the efficient light-harvesting hierarchical structures composed of MPs and NWs. The average R_{total} is reduced to 2.96% at wavelengths of 300−1100 nm by the hierarchical structures with only 1.16 μm long NWs, superior to the surfaces (without MPs) purely consisting of long NWs up to 40 μm in length, and R_{spec} is less than 0.23% at the AOI up to 70° for all the wavelengths. Excellent broad-band and omnidirectional light-harvesting characteristics of the hierarchical structures result from gradient refractive index effect by NWs combining with the scattering effect by MPs. We addressed one of the most important issues for putting high-efficiency nanostructured solar cells into practice: atomic smooth, defect- and contamination-free surfaces to minimize the interface/surface recombination rate in high-aspect-ratio nanostructures obtained *via* appropriate CPE treatments applied to hierarchical structures, giving rise to a concurrent improvement in electrical and optical characteristics of the radial junction architecture. As compared to MP ones, hierarchical SHJ cells exhibit a daily power enhancement (44.2%) 2 times higher than the power density enhancement at normal AOI (21.8%), demonstrating omnidirectional PV characteristics achieved by the photon management employing hierarchical structures. Such a hierarchical architecture concept offering

excellent broad-band and omnidirectional light-harvesting characteristics, significantly increased junction areas, and high carrier lifetimes indicates the future of nanostructured solar cells for developing scalable and cost-effective manufacture technology in the renewable energy industry.

METHODS

As-cut Cz n-type monocrystalline Si(001) wafers with a thickness of 200 μm were used. First, the Si MPs were fabricated *via* an anisotropic etching process using a solution of KOH and IPA at 85 °C. Subsequently, a Ag nanoparticle layer was deposited on the MPs using electron beam evaporation for metal-assisted chemical etching. The large-area and uniform hierarchical structures of MPs and NWs were obtained by immersing the Ag nanoparticle-covered micropyramidal substrates into the etching solution of $HF/H_2O_2/H_2O$ for 30−90 s at room temperature. Finally, the isotropic CPE treatment using HNO_3 and HF was carried out to remove the defects and metal contamination. All of the wafers were cleaned by standard RCA cleaning followed by 1% HF dipping.

For SHJ solar cell fabrication, the PECVD process was carried out at 150 °C for the deposition of an intrinsic a-Si:H buffer layer (5 nm)/p-type a-Si:H layer (6 nm) on top as emitter layers and an intrinsic a-Si:H buffer layer (5 nm)/n-type a-Si:H layer (10 nm) on the back as surface field layers. Finally, the ITO contacts were deposited on both sides by the sputtering method, followed by Ag grids on the top and a full coverage of Ag on the back using the electron beam evaporation.

Morphological and microstructure studies were performed with a JEOL 2100F TEM operating at 200 kV and a JEOL JSM-6500 field emission SEM. The substrate-bound NWs were mechanically scraped, sonicated in ethanol, and deposited on carbon-coated copper grids for TEM characterization. The reflectance measurements were carried out with a standard UV−vis spectrometer (JASCO ARN-733) with an integrating sphere. Following a-Si:H layer deposition on the both sides, effective carrier lifetimes were characterized using the QSSPC system (Sinton Instruments WCT-120). The *J*−*V* characteristics were carried out under the illumination of an AM 1.5G solar simulator at 100 mW/cm^{-2} with a Keithley 2400 source meter. The EQE measurements (Enlitech QE-R) were performed by coupling the halogen lamp to a monochromator.

Conflict of Interest: The authors declare no competing financial interest.

Acknowledgment. This work was supported by National Science Council of Taiwan (102-2628-M-002-006-MY3 and 101-2221-E-002-115-MY2) and National Taiwan University (10R70823). This work is dedicated to the memory of Professor Li-Jen Chou at National Tsing Hua University, who passed away on December 14th, 2012 before the completion of this work. Professor Chou has made significant contributions to nanoscale science and engineering and will be missed and remembered as a caring mentor and an outstanding scientist.

Supporting Information Available: Performance characteristics of n-type Si-based nanostructured solar cells are summarized in Table S1; SEM images of Si hierarchical structures with different CPE durations are presented Figure S1; Ag 3d XPS spectra for the surfaces of hierarchical structures are illustrated in Figure S2; schematic of hierarchical structured Si SHJ solar cells for FDTD simulations is illustrated in Figure S3; implied V_{oc} of all structures is illustrated in Figure S4. This material is available free of charge *via* the Internet at http://pubs.acs.org.

REFERENCES AND NOTES

1. Hsu, C. Y.; Lien, D. H.; Lu, S. Y.; Chen, C. Y.; Kang, C. F.; Chueh, Y. L.; Hsu, W. K.; He, J. H. Supersensitive, Ultrafast, and Broad-Band Light-Harvesting Scheme Employing Carbon Nanotube/TiO_2 Core−Shell Nanowire Geometry. *ACS Nano* **2012**, *6*, 6687–6692.
2. Tsai, D. S.; Lin, C. A.; Lien, W. C.; Chang, H. C.; Wang, Y. L.; He, J. H. Ultra-High-Responsivity Broadband Detection of Si Metal−Semiconductor−Metal Schottky Photodetectors Improved by ZnO Nanorod Arrays. *ACS Nano* **2011**, *5*, 7748–7753.
3. Wierer, J. J.; David, A.; Megens, M. M. III-Nitride Photonic-Crystal Light-Emitting Diodes with High Extraction Efficiency. *Nat. Photonics* **2009**, *3*, 163–169.
4. Zhu, J.; Yu, Z.; Fan, S.; Cui, Y. Nanostructured Photon Management for High Performance Solar Cells. *Mater. Sci. Eng. Rep.* **2010**, *70*, 330–340.
5. Lin, Q.; Hua, B.; Leung, S.-f.; Duan, X.; Fan, Z. Efficient Light Absorption with Integrated Nanopillar/Nanowell Arrays for Three-Dimensional Thin-Film Photovoltaic Applications. *ACS Nano* **2013**, *7*, 2725–2732.
6. Tsai, S. H.; Chang, H. C.; Wang, H. H.; Chen, S. Y.; Lin, C. A.; Chen, S. A.; Chueh, Y. L.; He, J. H. Significant Efficiency Enhancement of Hybrid Solar Cells Using Core−Shell Nanowire Geometry for Energy Harvesting. *ACS Nano* **2011**, *5*, 9501–9510.
7. Wei, W. R.; Tsai, M. L.; Ho, S. T.; Tai, S. H.; Ho, C. R.; Tsai, S. H.; Liu, C. W.; Chung, R. J.; He, J. H. Above-11%-Efficiency Organic−Inorganic Hybrid Solar Cells with Omnidirectional Harvesting Characteristics by Employing Hierarchical Photon Trapping Structures. *Nano Lett.* **2013**, *13*, 3658–3663.
8. Wang, H. P.; Lai, K. Y.; Lin, Y. R.; Lin, C. A.; He, J. H. Periodic Si Nanopillar Arrays Fabricated by Colloidal Lithography and Catalytic Etching for Broadband and Omnidirectional Elimination of Fresnel Reflection. *Langmuir* **2010**, *26*, 12855–12858.
9. Dai, Y. A.; Chang, H. C.; Lai, K. Y.; Lin, C. A.; Chung, R. J.; Lin, G. R.; He, J. H. Subwavelength Si Nanowire Arrays for Self-Cleaning Antireflection Coatings. *J. Mater. Chem.* **2010**, *20*, 10924–10930.
10. Lin, Y. R.; Lai, K. Y.; Wang, H. P.; He, J. H. Slope-Tunable Si Nanorod Arrays with Enhanced Antireflection and Self-Cleaning Properties. *Nanoscale* **2010**, *2*, 2765–2768.
11. Chang, H. C.; Lai, K. Y.; Dai, Y. A.; Wang, H. H.; Lin, C. A.; He, J. H. Nanowire Arrays with Controlled Structure Profiles for Maximizing Optical Collection Efficiency. *Energy Environ. Sci.* **2011**, *4*, 2863–2869.
12. Peng, K.-Q.; Lee, S.-T. Silicon Nanowires for Photovoltaic Solar Energy Conversion. *Adv. Mater.* **2011**, *23*, 198–215.
13. Kelzenberg, M. D.; Boettcher, S. W.; Petykiewicz, J. A.; Turner-Evans, D. B.; Putnam, M. C.; Warren, E. L.; Spurgeon, J. M.; Briggs, R. M.; Lewis, N. S.; Atwater, H. A. Enhanced Absorption and Carrier Collection in Si Wire Arrays for Photovoltaic Applications. *Nat. Mater.* **2010**, *9*, 239–244.
14. Adachi, M. M.; Anantram, M. P.; Karim, K. S. Core−Shell Silicon Nanowire Solar Cells. *Sci. Rep* **2013**, *3*, 1–6.
15. Jia, G.; Eisenhawer, B.; Dellith, J.; Falk, F.; Thøgersen, A.; Ulyashin, A. Multiple Core−Shell Silicon Nanowire-Based Heterojunction Solar Cells. *J. Phys. Chem. C* **2013**, *117*, 1091–1096.
16. Oh, J.; Yuan, H.-C.; Branz, H. M. An 18.2%-Efficient Black-Silicon Solar Cell Achieved through Control of Carrier Recombination in Nanostructures. *Nat. Nanotechnol.* **2012**, *7*, 743–748.
17. Garnett, E.; Yang, P. Light Trapping in Silicon Nanowire Solar Cells. *Nano Lett.* **2010**, *10*, 1082–1087.
18. Garnett, E. C.; Yang, P. Silicon Nanowire Radial p-n Junction Solar Cells. *J. Am. Chem. Soc.* **2008**, *130*, 9224–9225.
19. Kopecek, R.; Libal, J.; Buck, T.; Peter, K.; Wambach, K.; Acciarri, M.; Binetti, S.; Geerligs, L. J.; Fath, P. n-Type Multicrystalline Silicon: Material for Solar Cell Processes with High Efficiency Potential. In *31st IEEE Photovoltaic Specialists Conference*; Lake Buena Vista, FL, **2005**; pp 1257−1260.

20. Panasonic Corp. Panasonic HIT® Solar Cell Achieves World's Highest Conversion Efficiency of 24.7% at Research Level. http://panasonic.co.jp/corp/news/official.data/data.dir/2013/02/en130212-7/en130212-7.pdf, 2013.
21. Descoeudres, A.; Holman, Z. C.; Barraud, L.; Morel, S.; De Wolf, S.; Ballif, C. >21% Efficient Silicon Heterojunction Solar Cells On n- and p-Type Wafers Compared. *IEEE J. Photovoltaics* **2013**, *3*, 83–89.
22. Cuevas, A.; Kerr, M. J.; Samundsett, C.; Ferrazza, F.; Coletti, G. Millisecond Minority Carrier Lifetimes in n-Type Multicrystalline Silicon. *Appl. Phys. Lett.* **2002**, *81*, 4952–4954.
23. Glunz, S. W.; Rein, S.; Lee, J. Y.; Warta, W. Minority Carrier Lifetime Degradation in Boron-Doped Czochralski Silicon. *J. Appl. Phys.* **2001**, *90*, 2397–2404.
24. Geerligs, L. J.; Macdonald, D. Base Doping and Recombination Activity of Impurities in Crystalline Silicon Solar Cells. *Prog. Photovoltaics* **2004**, *12*, 309–316.
25. Chao, Y. C.; Chen, C. Y.; Lin, C. A.; He, J. H. Light Scattering By Nanostructured Anti-reflection Coatings. *Energy Environ. Sci.* **2011**, *4*, 3436–3441.
26. Kazmerski, L. L. Photovoltaics: A Review of Cell and Module Technologies. *Renewable Sustainable Energy Rev.* **1997**, *1*, 71–170.
27. Huang, Z.; Shimizu, T.; Senz, S.; Zhang, Z.; Zhang, X.; Lee, W.; Geyer, N.; Gösele, U. Ordered Arrays of Vertically Aligned [110] Silicon Nanowires by Suppressing the Crystallographically Preferred ⟨100⟩ Etching Directions. *Nano Lett.* **2009**, *9*, 2519–2525.
28. Huang, Z.; Geyer, N.; Werner, P.; de Boor, J.; Gösele, U. Metal-Assisted Chemical Etching of Silicon: A Review. *Adv. Mater.* **2011**, *23*, 285–308.
29. Olibet, S.; Monachon, C.; Hessler-Wyser, A.; Vallat-Sauvain, E.; Fesquet, L.; Damon-Lacoste, J.; De Wolf, S.; Ballif, C. Textured Silicon Heterojunction Solar Cells with Over 700 mV Open-Circuit Voltage Studied by Transmission Electron Microscopy. In *Proceedings of the 22nd EUPVSEC*; Valencia, Spain, **2008**; pp 1140−1144.
30. Wang, T. H.; Iwaniczko, E.; Page, M. R.; Levi, D. H.; Yan, Y.; Branz, H. M.; Wang, Q. Effect of Emitter Deposition Temperature on Surface Passivation in Hot-Wire Chemical Vapor Deposited Silicon Heterojunction Solar Cells. *Thin Solid Films* **2006**, *501*, 284–287.
31. Das, U. K.; Burrows, M. Z.; Lu, M.; Bowden, S.; Birkmire, R. W. Surface Passivation and Heterojunction Cells on Si (100) and (111) Wafers Using DC and RF Plasma Deposited Si:H Thin Films. *Appl. Phys. Lett.* **2008**, *92*, 063504.
32. Xiu, Y.; Zhu, L.; Hess, D. W.; Wong, C. P. Hierarchical Silicon Etched Structures for Controlled Hydrophobicity/Superhydrophobicity. *Nano Lett.* **2007**, *7*, 3388–3393.
33. Jia, G.; Steglich, M.; Sill, I.; Falk, F. Core−Shell Heterojunction Solar Cells on Silicon Nanowire Arrays. *Sol. Energy Mater. Sol. Cells* **2012**, *96*, 226–230.
34. Edwards, M.; Bowden, S.; Das, U. K.; Burrows, M. Effect of Texturing and Surface Preparation on Lifetime and Cell Performance in Heterojunction Silicon Solar Cells. *Sol. Energy Mater. Sol. Cells* **2008**, *92*, 1373–1377.
35. Schmidt, V.; Senz, S.; Gösele, U. Diameter-Dependent Growth Direction of Epitaxial Silicon Nanowires. *Nano Lett.* **2005**, *5*, 931–935.
36. Woo-Byoung, K. A.; Matsumoto, T.; Kobayashi, H. Ultrathin SiO_2 Layer on Atomically Flat Si (111) Surfaces with Excellent Electrical Characteristics Formed by Nitric Acid Oxidation Method. *Appl. Phys. Lett.* **2008**, *93*, 072101.
37. Kobayashi, H.; Imamura, K.; Kim, W. B.; Im, S. S. Asuha Nitric Acid Oxidation of Si (NAOS) Method for Low Temperature Fabrication of SiO_2/Si and SiO_2/SiC Structures. *Appl. Surf. Sci.* **2010**, *256*, 5744–5756.
38. Lien, S.-Y.; Yang, C.-H.; Hsu, C.-H.; Lin, Y.-S.; Wang, C.-C.; Wuu, D.-S. Optimization of Textured Structure on Crystalline Silicon Wafer for Heterojunction Solar Cell. *Mater. Chem. Phys.* **2012**, *133*, 63–68.
39. Xiu, Y.; Zhang, S.; Yelundur, V.; Rohatgi, A.; Hess, D. W.; Wong, C. P. Superhydrophobic and Low Light Reflectivity Silicon Surfaces Fabricated by Hierarchical Etching. *Langmuir* **2008**, *24*, 10421–10426.
40. Ozdemir, B.; Kulakci, M.; Turan, R.; Unalan, H. E. Effect of Electroless Etching Parameters on the Growth and Reflection Properties of Silicon Nanowires. *Nanotechnology* **2011**, *22*, 155606.
41. Li, H. F.; Jia, R.; Chen, C.; Xing, Z.; Ding, W. C.; Meng, Y. L.; Wu, D. Q.; Liu, X. Y.; Ye, T. C. Influence of Nanowires Length on Performance of Crystalline Silicon Solar Cell. *Appl. Phys. Lett.* **2011**, *98*, 151116.
42. Bullis, W. M.; Huff, H. R. Interpretation of Carrier Recombination Lifetime and Diffusion Length Measurements in Silicon. *J. Electrochem. Soc.* **1996**, *143*, 1399–1405.
43. Damon-Lacoste, J.; Labrune, M.; Granata, S.; Daineka, D.; Roca i Cabarrocas, P. Crystalline Silicon Solar Cells with Doped Epitaxial Silicon Films Obtained at Low-Temperature by PECVD. In *35th IEEE Photovoltaic Specialists Conference*; Honolulu, HI, **2010**; pp 001352−001357.
44. Kempa, T. J.; Cahoon, J. F.; Kim, S.-K.; Day, R. W.; Bell, D. C.; Park, H.-G.; Lieber, C. M. Coaxial Multishell Nanowires with High-Quality Electronic Interfaces and Tunable Optical Cavities for Ultrathin Photovoltaics. *Proc. Natl. Acad. Sci. U.S.A.* **2012**, *109*, 1409–1412.
45. Solanki, C. S. *Solar Photovoltaics: Fundamentals, Technologies and Applications*; PHI Leaning Private Ltd.: New Delhi, 2009.
46. Veschetti, Y.; Muller, J. C.; Damon-Lacoste, J.; Roca i Cabarrocas, P.; Gudovskikh, A. S.; Kleider, J. P.; Ribeyron, P. J.; Rolland, E. Improvement of Polymorphous/Crystalline Heterojunction Solar Cells Using Low Temperature Screen-Printed Pastes. In *31th IEEE Photovoltaic Specialists*, Lake Buena Vista, FL, **2005**; pp 1131−1134.
47. Sark, W. G. J. H. M.; Korte, L.; Roca, F. *Physics and Technology of Amorphous-Crystalline Heterostructure Silicon Solar Cells*; Springer-Verlag: Heidelberg, Germany, 2011; pp 180−181.